Measurements of Dipole Moments for the $5s5p\,^3P_1$–$5sns\,^3S_1$ Transitions via Autler–Townes Spectroscopy

Canzhu Tan[1,2], Fachao Hu[1,2], Zhijing Niu[1,2†], Yuhai Jiang[2,3*], Matthias Weidemüller[1,2,4*], and Bing Zhu[2,4,5*]

[1]*Hefei National Laboratory for Physical Sciences at the Microscale, University of Science and Technology of China, Hefei 230026, China*

[2]*CAS Center For Excellence in Quantum Information and Quantum Physics, University of Science and Technology of China, Hefei 230026, China*

[3]*Center for Transformative Science and School of Physical Science and Technology, ShanghaiTech University, Shanghai 201210, China*

[4]*Physikalisches Institut, Universität Heidelberg, Im Neuenheimer Feld 226, 69120 Heidelberg, Germany*

[5]*HSBC Lab-China, Guangzhou 510620, China*

(Received 30 June 2022; accepted manuscript online 11 August 2022)

We report on experimental measurements of the transition dipole moments (TDMs) between the intermediate state $5s5p\,^3P_1$ and the triplet Rydberg series $5sns\,^3S_1$ in an ultracold strontium gas. Here n is the principal quantum number ranging from 19 to 40. The transition $5s5p\,^3P_1$–$5sns\,^3S_1$ is coupled via an ultraviolet (UV) beam, inducing Autler–Townes splitting of both states. Such a splitting of the intermediate state is spectroscopically measured by using absorption imaging on a narrow transition $5s^2\,^1S_0$–$5s5p\,^3P_1$ in an ultracold gas of strontium atoms. The power and size of the UV beam are carefully determined, with which the TDMs are extracted from the measured Autler–Townes splitting. The experimentally obtained TDMs are compared to the calculations based on a parametric core potential, on a Coulomb potential with quantum defect, and on the open-source library Alkali Rydberg calculator, finding good agreement with the former two models and significant deviation with the latter.

DOI: 10.1088/0256-307X/39/9/093202

Rydberg atoms have many exaggerated properties,[1] e.g., the scaling of level energy, wavefunction, lifetime, and atom-atom interaction, with the principal quantum number n, enabling them active research frontiers in the fields of quantum simulations,[2,3] quantum information and quantum computing,[4] and emerging quantum technologies.[5] The study of Rydberg structure dates back to the early days of quantum mechanics in the context of quantitative atomic spectroscopy.[6] Nowadays, both single-particle properties and pairwise interactions for Rydberg states of alkali atoms can be routinely calculated using open-source libraries such as Alkali Rydberg calculator (ARC)[7] and Pairinteraction.[8] Recent developments of Rydberg physics with divalent atoms have been reviewed by Ref. [9].

Realizing strong and controllable couplings to one or several highly excited Rydberg states from a low-lying ground state using lasers is crucial in many aforementioned applications of Rydberg atoms. The coupling strength can be predicted quite accurately for alkali atoms using theoretical calculations based on the single-active-electron (SAE) approximation, such as pure Coulomb[10] or realistic model potentials,[7,11] and semi-classical method.[12] The SAE approximation is in general problematic for divalent atoms due to the large open-shell core polarizability and the existence of so-called doubly-excited "perturbers" there.[9] Nevertheless, the properties of highly excited Rydberg states in divalent atoms can be estimated using SAE methods in many cases,[13,14] while for observables involving low-lying states, theoretical methods taking two-electron correlations into consideration, such as configuration interaction expansion with a two-active-electron approximation[15] and multi-channel quantum defect theory,[16] are needed.

In this work, we report on systematic measurements of transition dipole moments (TDMs) of the $5s5p\,^3P_1$–$5sns\,^3S_1$ transitions in divalent strontium via Autler–Townes (AT) spectroscopy.[17] By performing absorption imaging on the narrow $5s^2\,^1S_0$–$5s5p\,^3P_1$ transition,[18] we probe the AT splitting of the meta-stable (lifetime ∼21 μs) $5s5p\,^3P_1$ state being coupled to the triplet Rydberg series $5sns\,^3S_1$ through an ultraviolet (UV) beam. Splittings as small as 150 kHz with a typical width of 200 kHz (FWHM, full width at half maximum) are measured with the principal quantum number n in the range of $19 \leq n \leq 40$. The measured TDMs are compared to three different theoretical calculations, two of which use the SAE approximation and agree quite well with our experimental results. Measuring TDMs of optical transitions via AT spectroscopy has been used in alkali[17,19] and molecular[20] systems and

†Current address: Department of Physics, University of Colorado Boulder

*Corresponding authors. Email: jiangyh@sari.ac.cn; weidemueller@uni-heidelberg.de; bzhu1990@gmail.com

© 2022 Chinese Physical Society and IOP Publishing Ltd

the extension to divalent atoms is performed here for the first time. Compared to other experimental methods of determining TDMs such as lifetime measurements, the AT-spectroscopy method directly accesses the TDMs without perturbations from systematic uncertainties.[21]

In this Letter, the experiments are described first, including the experimental apparatus, the spectroscopic measurements, and the analysis to extract the n-dependent TDMs. Then, the theoretical calculation and the comparison to experiments are presented. Finally, we give conclusions.

Experiments. Our experimental apparatus for laser cooling and trapping of strontium atoms has been described before in Refs. [22–24]. Briefly, ^{88}Sr atoms loaded from a two-dimensional magneto-optical trap (MOT)[22] are collected and cooled in a two-stage three-dimensional MOT operating on the broad $5s^2\,{}^1S_0$–$5s5p\,{}^1P_1$ and narrow $5s^2\,{}^1S_0$–$5s5p\,{}^3P_1$ transitions, respectively. At the end of the narrow-line MOT, a crossed optical dipole trap (ODT) at 532 nm is switched on to provide further trapping after the MOT phase. We hold the atoms in the ODT for several hundreds of milliseconds, after which a cloud of 10^5 atoms at 1 μK is typically obtained. The two ODT beams cross at an angle of 18° [as illustrated in Fig. 1, resulting a typical atom cloud size of (27, 69, 27) μm and a peak density of $7 \times 10^{11}\,\mathrm{cm}^{-3}$. Considering our stainless steel vacuum chamber with no nonconducting surfaces close to the atomic cloud,[25] we can ignore the effects of stray dc electric fields in all following experiments.

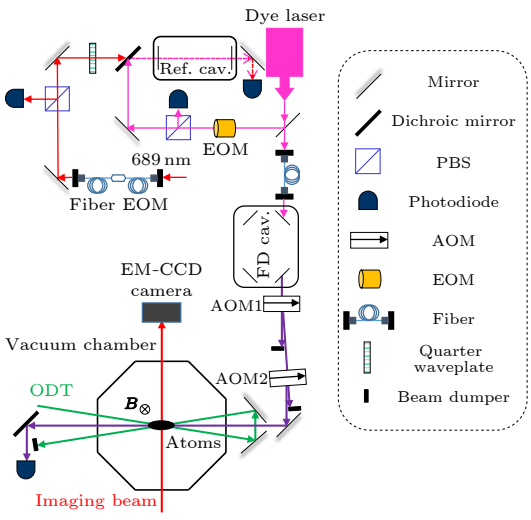

Fig. 1. Experimental setup. PBS: polarizing beam-splitter, AOM: acousto-optic modulator, EOM: electro-optic modulator, FD cav.: frequency-doubling cavity, Ref. cav.: reference cavity.

The triplet Rydberg series $5sns\,{}^3S_1$ ($\equiv |r\rangle$) has been spectroscopically studied in our recent work,[25] where a two-photon excitation scheme as shown in Fig. 2(a) was employed. The first photon at 689 nm driving the transition between the ground state $5s^2\,{}^1S_0$ ($\equiv |g\rangle$) and the meta-stable state $5s5p\,{}^3P_1$ ($\equiv |i\rangle$) is delivered from the narrow-line cooling laser, which is locked to an ultra-stable cavity.[24] This laser has a line width smaller than 10 kHz and a daily drift of 8 kHz/day.[24] The Rydberg states $|r\rangle$ are coupled to $|i\rangle$ by a UV light at 319 nm generated from a frequency-doubled dye laser, which is frequency stabilized to a low-finesse reference cavity via the Pound–Drever–Hall (PDH) technique [see Fig. 1] resulting in a linewidth of about 100 kHz. In Ref. [25], we measured the energy of Rydberg states via the atom-loss spectroscopy, where the number of atoms in the narrow-line MOT was measured as a function of the UV frequency. However, the determination of the UV resonance is limited by the Rydberg–Rydberg interactions in the atom-loss spectra,[26,27] especially for higher n.

To enable a finer tuning of the UV frequency as well as a better determination of the UV resonance, we implement the following two main upgrades compared to Ref. [25]: (i) As shown in Fig. 1, the length of reference cavity to which the dye laser locks is stabilized to a frequency-locked red light, where a fiber electro-optic modulator (EOM) is used to tune the cavity length, and hence the dye laser frequency. (ii) Instead of exciting enough Rydberg atoms to induce significant losses, here we measure the absorption properties on a weak probe beam through a cloud of ground state atoms in the presence of a strong UV light. Two acousto-optic modulators (AOM1 and AOM2 in Fig. 1) are inserted into the UV beam path to perform intensity stabilization (with AOM1) and fast switching (with AOM2). The absorption on the red beam is extracted with an EM-CCD camera (Andor iXon 897) using the standard absorption imaging sequence.[18] The narrowness of the 689-nm probe transition ($\sim 2\pi \times 7.5$ kHz) provides a sensitive measurement of both the UV resonance and the UV-induced ATS of $|i\rangle$.

We have already studied in detail the narrow-line absorption spectrum without the presence of UV light in Ref. [18], which can be described well by a symmetric Voigt profile with a small imaging intensity. In Fig. 2(b) we show such a spectrum measured by a large red imaging beam (a $1/e^2$ diameter of 4.2 mm) with an intensity of about $0.1I_\mathrm{s}$, in which an FWHM of 40(2) kHz is observed. Here $I_\mathrm{s} = 3\,\mu\mathrm{W/cm}^2$ is the saturation intensity for the $|g\rangle - |i\rangle$ transition. The observed spectrum width is dominated by the Doppler effect[18] and the position of the absorption peak represents the on-resonance condition of the red transition.

The Rydberg spectrum is measured by monitoring the absorption of an on-resonance 689-nm light in the presence of a UV beam as a function of the UV frequency. Both the red and UV beams propagate horizontally and they cross each other perpendicularly at the position of the atomic cloud. An external magnetic field of about 1 G is applied vertically, giving rise to a Zeeman splitting of about $h \times 4.86$ MHz (8.10 MHz) for the $|i\rangle$ ($|r\rangle$) state. The UV beam is vertically polarized to drive the $\Delta m = 0$ transition with m being the magnetic quantum number. The linear polarization of the red beam is horizontal and the red frequency is tuned to be resonant with the $\Delta m = +1$

transition, as seen in Fig. 2(a). The UV beam is switched on before applying the red one and its frequency is scanned via the fiber EOM (see Fig. 1).

As an example, a measurement for the $5s37s\,^3S_1$ state is shown in Fig. 2(c), where the same imaging conditions are used as in Fig. 2(b). We fit the spectrum to a Gaussian function to extract the resonance center and width. The UV resonance position is determined with an uncertainty of 13 kHz, and the FWHM is 461(32) kHz, which mainly comes from the UV power broadening (a Rabi frequency of about 350 kHz is used here). The minimum FWHM for such a spectrum we have obtained is about 200 kHz.

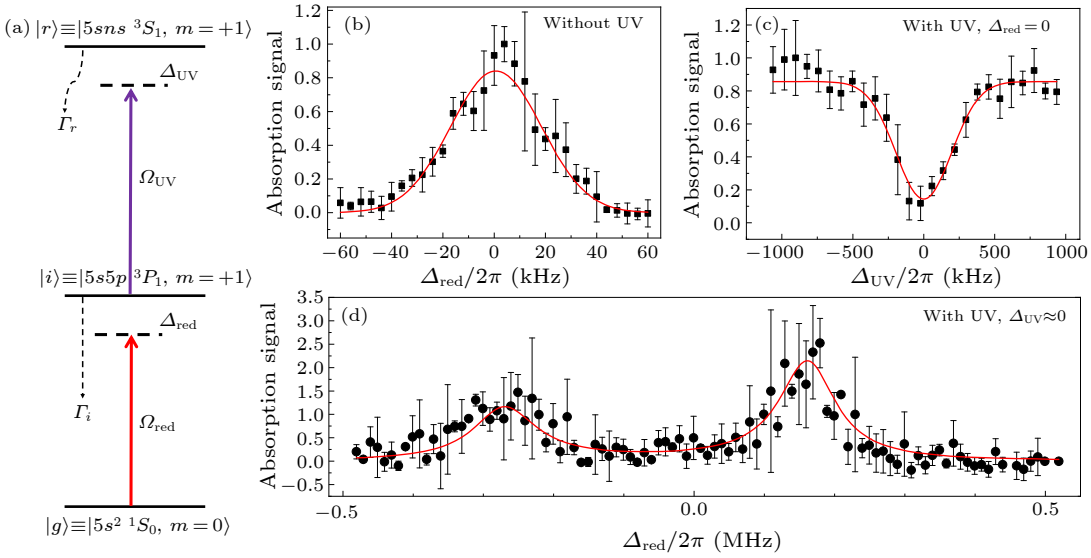

Fig. 2. Autler–Townes Spectroscopy: (a) Energy level scheme. The Rydberg state $|r\rangle$ is coupled to the meta-stable state $|i\rangle$ by a UV beam with a Rabi frequency $\Omega_{\rm UV}$ and a detuning $\Delta_{\rm UV}$. The lower state is probed via a red imaging beam driving the $|g\rangle-|i\rangle$ transition with Rabi frequency $\Omega_{\rm red}$ and detuning $\Delta_{\rm red}$. State $|i\rangle$ decays to $|g\rangle$ with a rate of Γ_i while the decay rate from the Rydberg state is Γ_r including that to $|i\rangle$. (b) Narrow-line absorption spectrum without the UV beam. The spectrum is measured with an intensity of $0.1I_{\rm s}$ and an imaging time of 200 µs. The error bars represent the standard deviation of five repeated measurements. The solid line is a fit to the Voigt profile to extract the spectrum center and width. (c) Rydberg spectroscopy. The absorption signal is recorded as a function of the applied UV frequency while keeping the red transition on resonance ($\Delta_{\rm red}=0$). The same imaging parameters used are the same as those in (b). The error bars are standard deviations of five measurements. A Gaussian function (solid line) is used to fit the spectrum to extract the on-resonance frequency of the UV transition and the corresponding width. See text for more details. (d) AT splitting of $|i\rangle$ induced by couplings to $|r\rangle$. The UV detuning is tuned to be close to resonance, and error bars are standard deviations of three repeats. The solid line is a fit to Eq. (1). See text for more details.

To characterize the coupling strength between $|i\rangle$ and $|r\rangle$, namely $\Omega_{\rm UV}$, we measure the narrow-line absorption imaging spectrum in the presence of a strong UV beam. A typical line shape is shown in Fig. 2(d) for $n=37$, which is fitted to an analytic formula [28]

$$\sigma\propto\frac{2(\bar{\Gamma}_i^2\bar{\Gamma}_r+4\bar{\Gamma}_r(\Delta_{\rm red}+\Delta_{\rm UV})^2+\bar{\Gamma}_i\Omega_{\rm UV}^2)}{4(\bar{\Gamma}_r\Delta_{\rm red}+\bar{\Gamma}_r\Delta_{\rm UV})^2+[\bar{\Gamma}_r\bar{\Gamma}_i-4\Delta_{\rm red}(\Delta_{\rm red}+\Delta_{\rm UV})+\Omega_{\rm UV}^2]^2},\tag{1}$$

where σ represents the absorption cross section and $\bar{\Gamma}_i=\Gamma_i+\gamma_{\rm red}$ and $\bar{\Gamma}_r=\Gamma_r+\gamma_{\rm UV}$ are the coherence decay rates for the two transitions, respectively; $\gamma_{\rm red}$ and $\gamma_{\rm UV}$ represent the dephasing effects like laser frequency noises, magnetic field fluctuations, and Doppler effect. By using the above formula we neglect any interaction-induced effect in the measured spectrum, which will be confirmed in the Supplementary material. All the parameters in Eq. (1) are freely fitted, including the UV near-zero UV detuning $\Delta_{\rm UV}$ to account for possible frequency drifts. From the fit we obtain $\Omega_{\rm UV}/2\pi=1.24(1)$ MHz, $\Delta_{\rm UV}/2\pi=0.072(6)$ MHz, $\bar{\Gamma}_i/2\pi=0.08(8)$ MHz, and $\bar{\Gamma}_r/2\pi=0.13(8)$ MHz.

The measured UV-induced ATS $\Omega_{\rm UV}$ is related to the UV intensity $I_{\rm UV}$ at the atomic cloud position via the TDM μ_n for the transition $|5s5p\,^3P_1,m_J=+1\rangle\rightarrow|5sns\,^3S_1,m_J=+1\rangle$, which reads

$$\Omega_{\rm UV}(r)=\frac{\mu\sqrt{2I_{\rm UV}(r)/c\epsilon_0}}{\hbar}.\tag{2}$$

Here c is the light speed in vacuum, ϵ_0 is the vacuum permittivity, $\hbar$ is the reduced Planck constant, and r is the atomic cloud position in the transverse direction. As plotted in Fig. 3(a), $\Omega_{\rm UV}$ is measured as a function of $I_{\rm UV}$ for six different n. On the one hand, the UV beam intensity $I_{\rm UV}$ must be carefully calibrated to quantitatively extract the TDM by fitting the measurements to Eq. (2). On the other hand, the frequency-doubling cavity shown in Fig. 1 needs to be realigned each time when changing n, and thus the UV beam profile and power change accordingly.

For each n, the UV power is recorded by a commercial power meter (S120VC, Thorlabs) with a measurement

uncertainty of 5%. The UV beam profile $I_{\rm UV}(x, y)$ in the plain of the atomic position is measured by a commercial beam profiler (from DataRay) with a pixel size of 12.9 µm. Since the size of atomic cloud (∼27 µm) is much smaller than the UV beam size (≥300 µm), we can safely assume an uniform intensity across the atomic cloud. Although we have carefully aligned the UV beam by maximizing the measured $\Omega_{\rm UV}$ at a fixed UV power, a largest deviation of $0.5w$ from the beam center is attributed to the atomic position, leading to a deviation of 30–50% of the maximum intensity. Here w is the beam waist by fitting the measured intensity profile to a Gaussian one. The intensities shown in Fig. 3(a) are the mean values considering these deviations. The solid lines are fits to Eq. (2) and the TDMs are obtained as shown in Fig. 4. A further treatment taking into account the non-uniform atomic density distribution is presented in the Supplementary material, which gives a small correction (∼10%) to the obtained intensity.

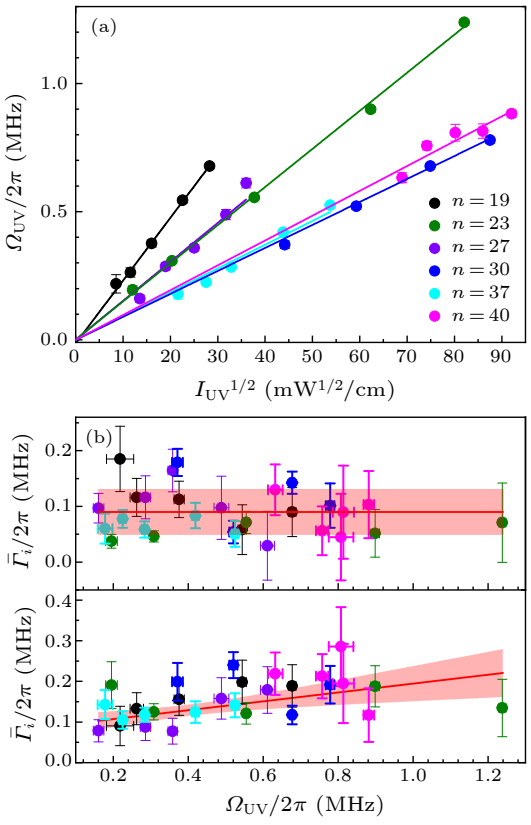

Fig. 3. Extracting experimental TDMs: (a) Measurements of the intensity-dependent AT splitting for six different n. Solid lines are fits to Eq. (2) to extract the TDMs. (b) Decoherence rates as a function of $\Omega_{\rm UV}$. In the upper panel, the $|i\rangle - |g\rangle$ decoherence rate $\bar{\Gamma}_i$ is independent of $\Omega_{\rm UV}$ and an average of $2\pi \times 0.09$ MHz is indicated by the horizontal line. The shaded area represents the standard deviation. In the lower panel, the $|r\rangle - |i\rangle$ decoherence rate $\bar{\Gamma}_r$ seems to be correlated with $\Omega_{\rm UV}$ and a fit to linear function gives a slope of 0.11(3) and an intercept of $2\pi \times 0.08(1)$ MHz. The shade area also shows the 95% confidence band.

The extracted TDMs are plotted in Fig. 4 with the solid dots representing results obtained from Fig. 3(a) and the shaded area showing the uncertainty from both the power and intensity profile measurements discussed above. Next, we will compare the measurements with three different theoretical calculations. Apart from extracting the TDMs from the measurements, we also show in Fig. 3(b) the obtained decoherence rates $\bar{\Gamma}_i$ (upper panel) and $\bar{\Gamma}_r$ (lower panel) as a function of the UV Rabi frequency $\Omega_{\rm UV}$. The $|i\rangle$–$|g\rangle$ decoherence rates are largely independent of $\Omega_{\rm UV}$ and an average value of $\sim 2\pi \times 90$ kHz is obtained, as indicated by the horizontal line. The shaded area represents the standard deviation. The decoherence rate $\bar{\Gamma}_r$ seems to be correlated with $\Omega_{\rm UV}$ and a minimum linear fit gives a slope of 0.11(3) and an intercept of $2\pi \times 0.08(1)$ MHz. The former may result from the inhomogeneous atomic density and beam intensity and the latter agrees well with our UV laser linewidth.

Comparison to Theoretical Calculations. As perturbations are weak for high-lying Rydberg states in the $5sns\,{}^3S_1$ series of strontium [16] and precise spectroscopic data is available, [25] SAE models are used here for calculating the $5s5p\,{}^3P_1$–$5sns\,{}^3S_1$ TDM. Under this approximation, the good quantum numbers are the electron orbit L, spin S, and total angular momentum J, and the concerned TDM between states $|5sns\,{}^3S_1, m_J = +1\rangle$ and $|5s5p\,{}^3P_1, m_J = +1\rangle$ is calculated as

$$\mu_n = \mu_\theta \int_{r_0}^{r_1} R_n(r) r R_i(r) dr, \tag{3}$$

where r is the electron-core distance and R_n (R_i) is the radial wavefunctions for the Rydberg (metastable) state. The angular part of the TDM $\mu_\theta = \frac{1}{\sqrt{2}}\langle L = 0, m_L = 0|\sqrt{\frac{4\pi}{3}} T_1^0 |L = 1, m_L = 1\rangle$ is $1/\sqrt{6}$. Here $|L, m_L\rangle$ are spherical harmonics and T_1^0 is the spherical tensor operator of rank 1 for π transition.

One method to calculate the radial wavefunctions is to consider a moving electron in the field of Sr^+ core and solve the Schödinger equation numerically with a parametric model potential in Klapisch form [29]

$$V_{\rm mod}(r) = -\frac{1}{r} - \frac{(Z-1)e^{-ar}}{r} + be^{-cr}, \tag{4}$$

where Z is the atomic number, and a, b, c are parameters to reproduce the experimental quantum defects, which are taken from Ref. [30]. The parameters for ${}^3S_1$ (${}^3P_1$) are $a = 2.93$ (3.35), $b = -5.28$ (−6.13), and $c = 1.22$ (1.12), respectively, with which the radial Shrödinger equation is solved using the Numerov algorithm [31] (see the Supplementary material). The TDM calculated with the model potential method is shown in Fig. 4 as red squares, where the short- (r_0) and long-range (r_1) cutoffs in Eq. (3) are 0.001 and $2n(n + 15)$ (in atomic unit), respectively, which are determined practically. [1]

Due to the fact that the second and third terms in Eq. (4) decay exponentially as r increases, the model potential differs significantly from a pure Coulomb potential [the first term in Eq. (4)] only at small r. For high-lying Rydberg levels, their wavefunctions are dominated

at large r such that calculations of $R_n(r)$ from a pure Coulomb potential are expected to be almost the same as those from Eq. (4). In Fig. 4, we plot the calculated TDMs (blue triangles) μ_n in Eq. (3) with $R_n(r)$ computed from a pure Coulomb potential using the experimentally measured quantum defects, $\delta(n) = \delta_0 + \frac{\delta_2}{(n-\delta_0)^2} + \frac{\delta_4}{(n-\delta_0)^4}$ with $\delta_0 = 3.37$, $\delta_2 = 0.418$, and $\delta_4 = -0.3$ for the $^3S_1$ Rydberg series.[25] $R_i(r)$ is still calculated using the corresponding model potential. The results are slightly larger than that from the model potential calculation and the differences become smaller for higher n (a maximum deviation of 3% at $n = 19$).

As a comparison, we also show in Fig. 4 the TDMs directly obtained from the open-source library ARC (Alkali Rydberg Calculator, available from https://arc-alkali-rydberg-calculator.readthedocs.io/)[32] as magenta diamonds, which uses a semi-classical approximation.[12] Such calculations are expected to give large errors for low-lying states (like $5s5p\,^3P_1$ here) since the semi-classical method cannot capture the effect of electron tunnelling into the core.

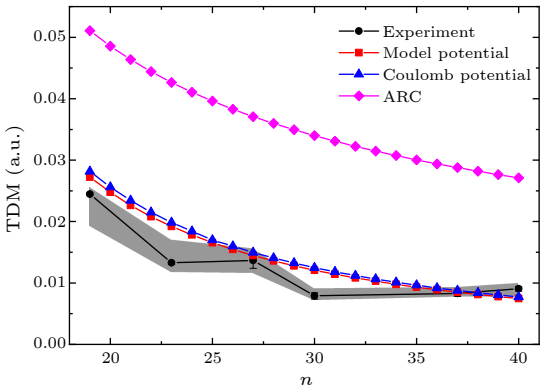

Fig. 4. TDMs for n range from 19 to 40. The black dots are the experimental results with the shaded area representing the uncertainties of the measurements coming from calibrations of the UV beam power and size. Error bars are from fittings in Fig. 3(a). The red squares, blue triangles, and magenta diamonds are theoretical calculations using the model potential, Coulomb potential, and semi-classical methods, respectively.

Comparing our experimental results to the above three theoretical calculations, the measured TDMs agree well with the calculations using both the model and Coulomb potentials with a maximum deviation of 35% for $n = 30$. The good agreements achieved here indicates that the SAE approximation may still be reasonably used to calculate wavefunctions of the low-lying states in divalent atoms. The results from the semi-classical method lie much higher than both the other theoretical values and the measurements, which is as expected due to the aforementioned reason. Deviations of measurements from the model- and Coulomb-potential values may result from uncertainties of both sides: The experimental results are limited by finite frequency resolution, power and size calibrations of the UV beam, and other mechanisms like Rydberg–Rydberg interactions (see the Supplementary material) affecting the lineshape Eq. (1), while the theoretical calculations of atomic wavefunctions are also not exact, i.e., the SAE approximation is used.

In summary, we have measured TDMs for the strontium $5s5p\,^3P_1$–$5sns\,^3S_1$ transitions for $19 \leq n \leq 40$ and found good agreements between the experimental results and calculations based on the SAE approximation. Our measurements can be extended to lower n states or other Rydberg series like $^3D_{1,2}$, to map out stronger two-electron effects. Furthermore, such high-resolution spectroscopy can also be used to determine Rydberg–Rydberg interactions in the current setup, which is interesting for future work.

Acknowledgements. We acknowledge helpful discussions with S. Yoshida, J. Burgdörfer and J. Zeng. This work was supported by the Anhui Initiative in Quantum Information Technologies. Y. H. Jiang also acknowledges support from the National Natural Science Foundation of China (Grant No. 11827806).

References

[1] Gallagher T F 2005 *Rydberg Atoms* (Cambridge: Cambridge University Press)
[2] Browaeys A and Lahaye T 2020 *Nat. Phys.* **16** 132
[3] Altman E, Brown K R, Carleo G, Carr L D, Demler E, Chin C, DeMarco B, Economou S E, Eriksson M A, Fu K M C, Greiner M, Hazzard K R, Hulet R G, Kollár A J, Lev B L, Lukin M D, Ma R, Mi X, Misra S, Monroe C, Murch K, Nazario Z, Ni K K, Potter A C, Roushan P, Saffman M, Schleier-Smith M, Siddiqi I, Simmonds R, Singh M, Spielman I, Temme K, Weiss D S, Vučković J, Vuletić V, Ye J, and Zwierlein M 2021 *PRX Quantum* **2** 017003
[4] Saffman M, Walker T G, and Mølmer K 2010 *Rev. Mod. Phys.* **82** 2313
[5] Adams C S, Pritchard J D, and Shaffer J P 2020 *J. Phys. B* **53** 012002
[6] White H E 1934 *Introduction to Atomic Spectra* (New York: McGraw-Hill)
[7] Šibalić N, Pritchard J D, Adams C S, and Weatherill K J 2017 *Comput. Phys. Commun.* **220** 319
[8] Weber S, Tresp C, Menke H, Urvoy A, Firstenberg O, Büchler H P, and Hofferberth S 2017 *J. Phys. B* **50** 133001
[9] Dunning F B, Killian T C, Yoshida S, and Burgdörfer J 2016 *J. Phys. B* **49** 112003
[10] Seaton M J 2002 *Comput. Phys. Commun.* **146** 225
[11] Marinescu M, Sadeghpour H R, and Dalgarno A 1994 *Phys. Rev. A* **49** 982
[12] Oumarou B, Picart J, Minh N T, and Chapelle J 1988 *Phys. Rev. A* **37** 1885
[13] Millen J, Lochead G, Corbett G R, Potvliege R M, and Jones M P A 2011 *J. Phys. B* **44** 184001
[14] Vaillant C L, Jones M P A, and Potvliege R M 2012 *J. Phys. B* **45** 135004
[15] Ye S, Zhang X, Killian T C, Dunning F B, Hiller M, Yoshida S, Nagele S, and Burgdörfer J 2013 *Phys. Rev. A* **88** 043430
[16] Vaillant C L, Jones M P A, and Potvliege R M 2014 *J. Phys. B* **47** 155001
[17] Piotrowicz M J, MacCormick C, Kowalczyk A, Bergamini S, Beterov I I, and Yakshina E A 2011 *New J. Phys.* **13** 093012

[18] Hu F, Tan C, Jiang Y, Weidemüller M, and Zhu B 2022 *Chin. Phys. B* **31** 016702

[19] Zhang H, Wang L, Chen J, Bao S, Zhang L, Zhao J, and Jia S 2013 *Phys. Rev. A* **87** 033835

[20] Ahmed E H, Huennekens J, Kirova T, Qi J, and Lyyra A M 2012 *Advances in Atomic, Molecular, and Optical Physics* (Amsterdam: Elsevier) vol 61 pp 467–514

[21] Sobelman I I 1992 *Atomic Spectra and Radiative Transitions* (Berlin: Springer)

[22] Nosske I, Couturier L, Hu F, Tan C, Qiao C, Blume J, Jiang Y H, Chen P, and Weidemüller M 2017 *Phys. Rev. A* **96** 053415

[23] Hu F, Nosske I, Couturier L, Tan C, Qiao C, Chen P, Jiang Y H, Zhu B, and Weidemüller M 2019 *Phys. Rev. A* **99** 033422

[24] Qiao C, Tan C Z, Hu F C, Couturier L, Nosske I, Chen P, Jiang Y H, Zhu B, and Weidemüller M 2019 *Appl. Phys. B* **125** 215

[25] Couturier L, Nosske I, Hu F, Tan C, Qiao C, Jiang Y H, Chen P, and Weidemüller M 2019 *Phys. Rev. A* **99** 022503

[26] Aman J A, DeSalvo B J, Dunning F B, Killian T C, Yoshida S, and Burgdörfer J 2016 *Phys. Rev. A* **93** 043425

[27] DeSalvo B J, Aman J A, Gaul C, Pohl T, Yoshida S, Burgdörfer J, Hazzard K R A, Dunning F B, and Killian T C 2016 *Phys. Rev. A* **93** 022709

[28] Fleischhauer M, Imamoglu A, and Marangos J P 2005 *Rev. Mod. Phys.* **77** 633

[29] Klapisch M 1971 *Comput. Phys. Commun.* **2** 239

[30] Millen J 2011 *A Cold Strontium Rydberg Gas*, Ph.D. thesis (Durham University)

[31] Johnson B R 1977 *J. Chem. Phys.* **67** 4086

[32] Robertson E J, Šibalić N, Potvliege R M, and Jones M P A 2021 *Comput. Phys. Commun.* **261** 107814

Supplementary matrial: Measurements of the transition dipole moments for the $5s5p\,^3P_1$-$5sns\,^3S_1$ transitions via Autler-Townes spectroscopy

Canzhu Tan,[1,2] Fachao Hu,[1,2] Zhijing Niu,[1,2,*] Yuhai Jiang,[3,2,†] Matthias Weidemüller,[1,2,4,‡] and Bing Zhu[4,2,5,§]

[1] *Hefei National Laboratory for Physical Sciences at the Microscale, University of Science and Technology of China, Hefei, Auhui 230026, China*
[2] *CAS Center For Excellence in Quantum Information and Quantum Physics, University of Science and Technology of China, Hefei, Anhui 230026, China*
[3] *Center for Transformative Science and School of Physical Science and Technology, ShanghaiTech University, Shanghai 201210, China*
[4] *Physikalisches Institut, Universität Heidelberg, Im Neuenheimer Feld 226, 69120 Heidelberg, Germany*
[5] *HSBC Lab-China, Guangzhou 510620, China*

(Dated: August 18, 2022)

A. The spatial-dependence of the AT splitting

Both the inhomogeneous atomic density and intensity distribution cause inhomogeneity on the observed AT splitting, which can be described as

$$\Omega_{\rm UV} \propto \langle\sqrt{I}\rangle = \int \sqrt{I(x,y)}n(x,y)dxdy\,, \tag{S1}$$

where $n(x,y)$ is the normalized column atomic density distribution, which is approximately a two-dimensional normal Gaussian function $f(x,y) = \frac{1}{2\pi\sigma_0^2}e^{-[(x-x_0)^2+(y-y_0)^2]/2\sigma_0^2}$ with the atomic cloud size $\sigma_0 = 27\,\mu$m. An uncertainty of $0.5(w_x, w_y)$ is attributed to the position of peak density (x_0, y_0), where w_x and w_y are the waists of UV beam obtained by fitting the intensity profile to a two-dimensional Gaussian function. So the integral in Eq. (S1) is calculated when scanning (x_0, y_0) pixel by pixel in a rectangular area with a size of $w_x \times w_y$ centered at the maximum beam intensity. The mean value of the resulting 1D data array can be used as the intensity in extracting the TDM, while the maximum and minimum give the upper and lower bound of the TDM measurement.

For the data plotted in Fig. 3(a), the intensity is obtained by neglecting the inhomogeneous atomic density distribution and keeping the attributed uncertainty for (x_0, y_0). This leads to a slightly larger intensity compared to the Eq. (S1) ($\sim 10\%$).

B. The Rydberg-Rydberg interaction in the AT spectrum

The strong Rydberg-Rydberg interaction gives rise to peak shift, asymmetry, additional dephasing in the AT spectrum, as observed previously [1–3]. These effects can be described on the mean-field level by the following interaction term [4, 5]

$$V = C_6(\frac{4\pi}{3}f_r n_0)^2\,, \tag{S2}$$

where the van der Waals coefficients C_6 range from $0.016\,\text{MHz}\cdot\mu\text{m}^6$ ($n = 19$) to $1420.5\,\text{MHz}\cdot\mu\text{m}^6$($n = 40$) [6] in our experiment, f_r is the Rydberg fraction, and n_0 is the ground state atom density. f_r in the strongly interacting case should be smaller than the noninteracting value, which is about 0.1% under our experimental conditions, due to the Rydberg blockade effect [3]. The interaction energy V in Eq. (S2) is about $2\pi\times 12\,$kHz with the noninteracting f_r value, which is much smaller than the observed AT splitting in our measurements. The interaction-induced dephasing rate is on the same order as the interaction term [2, 3], which is also small compared to the experimentally determined dephasing rates in Fig. 3(b).

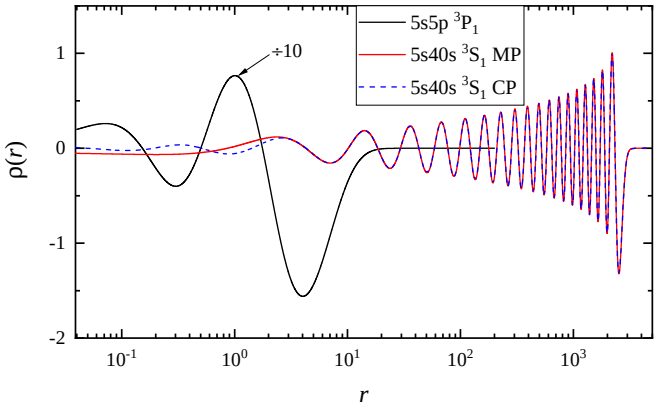

FIG. S1. Numerical results of the electronic wavefunctions. The black solid line is the wavefunction of the $5s5p\,^3P_1$ state calculated with the model potential (MP). The red solid and blue dashed lines are that of $5s40s\,^3S_1$ calculated with the MP and Coulomb potential (CP), respectively.

* Current address: Department of Physics, University of Colorado Boulder
† jiangyh@sari.ac.cn
‡ weidemueller@uni-heidelberg.de
§ bzhu1990@gmail.com

C. Numerov algorithm for solving radial Schrödinger equation

The radial Schrödinger equation under the SAE approximation reads as

$$\frac{d^2\rho(r)}{d^2r} = f(E,l,r)\rho(r), \tag{S3}$$

where $\rho(r) = rR(r)$ and $f(E,l,r) = -2E+2V(r)+\frac{l(l+1)}{r^2}$. Here r is the radial distance, $R(r)$ represents the radial wavefunction, E is the Energy, $V(r)$ is the electron-core interaction potential, and $\frac{l(l+1)}{r^2}$ is the centrifugal potential with the orbital angular momentum quantum number l. This one-variable quadratic differential equation can be numerically solved using the Numerov algorithm, which propagates $\rho(r)$ according to

$$\rho_{n+1}(1-\frac{h^2}{12}f(E,l,r_{n+1})) = 2\rho_n(1+\frac{5h^2}{12}f(E,l,r_n)) - \rho_{n-1}(1-\frac{h^2}{12}f(E,l,r_{n-1}))\,, \tag{S4}$$

where the radial variable r is discretized evenly with $h = r_n - r_{n-1}$ the step length and $\rho_n = \rho(r_n)$ is the discrete radial wavefunction.

For $V(r) = V_{mod}(r)$, the Eq. (S3) is solved for the bound-state problem, i.e. the bound-state energies are obtained consistently using matching conditions [7]. In the case of the Coulomb potential $V(r) = -1/r$ for the Rydberg wavefunctions, the bound-state energies E in Eq. (S3) are determined by experimental values [8]. As examples, Fig. S1 shows the numerically obtained radial wavefunctions for the low-lying $5s5p\,^3P_1$ and the Rydberg $5s40s\,^3S_1$ states.

[1] S. Sevinçli, C. Ates, T. Pohl, H. Schempp, C. S. Hofmann, G. Günter, T. Amthor, M. Weidemüller, J. D. Pritchard, D. Maxwell, A. Gauguet, K. J. Weatherill, M. P. A. Jones, and C. S. Adams, Journal of Physics B: Atomic, Molecular and Optical Physics **44**, 184018 (2011).

[2] J. Han, T. Vogt, and W. Li, Physical Review A **94**, 043806 (2016).

[3] B. J. DeSalvo, J. A. Aman, C. Gaul, T. Pohl, S. Yoshida, J. Burgdörfer, K. R. A. Hazzard, F. B. Dunning, and T. C. Killian, Physical Review A **93**, 022709 (2016).

[4] S. Helmrich, A. Arias, and S. Whitlock, Physical Review A **98**, 022109 (2018).

[5] J. de Hond, R. van Bijnen, S. J. J. M. F. Kokkelmans, R. J. C. Spreeuw, H. B. v. L. van den Heuvell, and N. J. van Druten, Physical Review A **98**, 062714 (2018).

[6] C. L. Vaillant, M. P. A. Jones, and R. M. Potvliege, Journal of Physics B: Atomic, Molecular and Optical Physics **45**, 135004 (2012).

[7] B. R. Johnson, The Journal of Chemical Physics **67**, 4086 (1977).

[8] L. Couturier, I. Nosske, F. Hu, C. Tan, C. Qiao, Y. H. Jiang, P. Chen, and M. Weidemüller, Physical Review A **99**, 022503 (2019).